Environ Monit Assess (2021) 193: 7
https://doi.org/10.1007/s10661-020-08769-2

Development of a mobile platform for monitoring gaseous, particulate, and greenhouse gas (GHG) pollutants

Tian Xia · James Catalan · Chris Hu · Stuart Batterman

Received: 12 October 2020 / Accepted: 18 November 2020 / Published online: 12 December 2020

Abstract The Michigan Pollution Assessment Laboratory (MPAL) is a mobile air quality monitoring platform designed to measure conventional, toxic, and greenhouse gas (GHG) air pollutants. The spatially and temporally resolved data collected can be used for multiple purposes, such as mapping spatial patterns and identifying peaks. The truck-based platform includes instrumentation for 11 gaseous pollutants and for particulate matter (PM), size distribution (7 nm to 20 μm), PM_{10}, black and brown carbon, and trace metals. MPAL is equipped with meteorological instruments, a high-accuracy GPS, forward and reverse cameras, and a data logging and display system. We selected commercially available instrumentation based on sensitivity, response time, and robustness. The vehicle's power system allows ~ 6.5 h of continuous operation with all instruments operating. This article details the design, construction, and evaluation of MPAL and summarizes data collected in its first year (March 2019 to March 2020) of operation. We completed a series of runs on 84 days in Detroit, Michigan, an area with a diverse set of traffic, industrial, and commercial emission sources, and collected 265,816 1-s observations (excluding collocations, zero checks, and other quality assurance measurements). Using data from these runs as well as special tests, we present results of performance evaluations that examined the response time, PM losses, and wind measurements and compare results to stationary regulatory monitoring data. We highlight key issues and provide practical solutions to help evaluate and resolve these issues and share many lessons learned in developing and using a mobile platform.

Keywords Air quality monitoring · Mobile · Pollutant mapping · Gas pollutants · Particulate matter (PM) · Greenhouse gas (GHG)

Introduction

Spatially and temporally resolved information on ambient air quality can reduce exposure measurement error in health studies, improve risk and disease burden projections in health impact and accountability studies, and better identify culpable sources in apportionment studies. In urban and industrial areas, air quality can exhibit considerable spatial and temporal variation, a result of different and highly variable emission sources and changing meteorology conditions. Considering $PM_{2.5}$, for example, local emission sources include thermal power plants and other industry, vehicle exhaust, tire and brake wear, biomass fires, and entrained dust, among others, while regional sources include distant emission sources. Conventional monitoring stations, usually established for regulatory purposes, are spatially

T. Xia (✉) · J. Catalan · S. Batterman
Department of Environmental Health Sciences, School of Public Health, University of Michigan, Ann Arbor, MI, USA
e-mail: xiatian@umich.edu

C. Hu
Department of Electrical Engineering and Computer Science, College of Engineering, University of Michigan, Ann Arbor, MI, USA

sparse and measure only selected pollutants and provide little information regarding spatial variation. Remote sensing data, most commonly using satellite data to estimate pollutant concentrations, can be used for several pollutants, but provide column-integrated measurements at relatively coarse spatial resolution (Duncan et al. 2014). Dispersion models can provide spatial and temporal information, but gaps in source inventories and other limitations increase uncertainties and can lead to errors.

The use of mobile platforms to measure spatial variation and detect peaks or "hotspots" of air pollutants has emerged as a monitoring approach that complements stationary monitors and remote sensing. Mobile monitoring has been used for a variety of purposes over the past two decades. Table 1 summarizes prior studies, which tend to fall into several groups. Most studies have examined the spatial distribution of ambient concentrations (Bukowiecki et al. 2002; Westerdahl et al. 2005; Westerdahl et al. 2008; Fruin et al. 2008; Wallace et al. 2009; Adams et al. 2012; Hagler et al. 2010; Baldauf et al. 2016; Levy et al. 2014b; Levy et al. 2014a; Elen et al. 2013; Van den Bossche et al. 2015; Apte et al. 2017). For example, in 2002–2003, Bukowiecki et al. (2002) and Westerdahl et al. (2005) integrated over 10 instruments into their mobile platforms to measure gaseous and particulate pollutants, meteorological and position data in Zurich, Switzerland, and Los Angeles, US, respectively. A second application is the estimation of on-road emissions using the "vehicle chasing" technique (Wang et al. 2009; Lee et al. 2015; Westerdahl et al. 2009; Wang et al. 2011; Wang et al. 2012), and the estimation of on-road passenger exposure (Kittelson et al. 2004; Yamada et al. 2016). Recently, low-cost sensors have been mounted on bicycles and backpacks to measure near-road concentrations and assess exposures of pedestrians and cyclists to traffic-related and other pollutants (Elen et al. 2013; Chan et al. 2002; Hatzopoulou et al. 2013; Minet et al. 2018). In rural areas, mobile systems have been used to estimate emissions from agricultural activities (Eilerman et al. 2016; Wild et al. 2017) and landfills (Hernandez Bennetts et al. 2012). NO_x, black carbon, and methane (CH_4) monitors have been mounted on Google Street View cars to map pollutant levels, and pipeline leaks of methane have been detected and quantified (Apte et al. 2017; von Fischer et al. 2017; Weller et al. 2018; Weller et al. 2019). Most field campaigns using mobile platforms have been short in duration, often just a few days (although several lasted months to a year) (Bukowiecki et al. 2002; Levy et al. 2014a; Levy et al. 2014b; Apte et al. 2017), and most have focused on a single pollutant.

Objectives

This study describes the design, development, and evaluation of a mobile platform for air quality monitoring called the Michigan Pollution Assessment Laboratory (MPAL). We highlight several important issues, e.g., potential biases in PM measurements and the effect of vehicle speed, and provide practical techniques that can evaluate and resolve these issues. Our intention is to share the many lessons learned in developing and using a mobile platform.

Material and methods

Design goals

The design for MPAL had multiple goals. (1) We wanted to measure a wide range of parameters, including criteria, toxic and greenhouse pollutants, as well as meteorological and position variables. (2) We preferred reasonably reliable and rugged, automated, and commercially available instruments with sufficient sensitivity for ambient measurements. Instruments meeting U.S. Environmental Protection Agency Federal Reference Methods (FRM) or Federal Equivalent Methods (FEMs), where applicable, were desirable, as were other instruments with technical support and known performance. (3) We desired high time resolution, ideally obtaining 1-s measurements, to allow mapping and other applications while driving at normal speeds. Because many parameters cannot be measured at this rate, at least with relatively economical instruments, this goal was flexible. (4) Instrument characteristics, including ancillary requirements, had to fall within a number of constraints, including physical size, power requirements, inlet flows, and the need for external pumps and compressed gases. Given safety, space, and logistics issues, we opted not to carry onboard gas cylinders. (5) We wanted to provide an appropriate environment for the instruments, specifically which reduced or controlled vibration, shocks, temperature swings, and condensation; noise inside the vehicle was also a factor. (6) A

Table 1 Summary of studies using mobile monitoring, listed by research group and date

Study	Purpose	Platform	Pollutants	Location	Time
Bukowiecki et al. 2002	Spatial and temporal distribution of gas pollutants and PM	IVECO Turbo Daily Transporter	PSD (7 nm – 20 μm); PNC; active surface area; black carbon (BC); $PM_{2.5}$; CO, CO_2; O_3; NO_x, NO_y, HNO_3, PAN; H_2O_2; HCHO; GPS; meteorology	Zürich, Switzerland	Feb 2001 -May 2002
Chan et al. 2002	Exposure in public transportation	Carried by lab staff as passengers	PM_{10}, $PM_{2.5}$, CO, CO_2	Guangzhou, China	May, Dec 2001
Kittelson et al. 2004	Exposure to on-road aerosols	Volvo tractor	PSD (<10 nm – 1 μm); PNC	Buffalo, NY, US	Sep 2002
Westerdahl et al. 2005, 2008; Fruin et al. 2008	Ultrafine particles (UFP); spatial variation	1998 Electric Toyota RAV4 SUV	UFP PNC (7 nm – 1 μm, particle length; BC; PSD (5 to 600 nm); particulate matter–phase PAH; $PM_{2.5}$; NO, NO_2, NO_x; CO, CO_2; Temperature, RH; GPS	Los Angeles, CA, US	Feb - Apr 2003
Wang et al. 2009, 2011, 2012; Westerdahl et al. 2009	On-road vehicle emission factors; chasing	A gasoline-powered minivan	CO, CO_2; BC; NO, NO_2, NO_x; PSD (5.6 – 560 nm), PM concentrations; relative humidity (RH) and temperature; GPS	Beijing and Chongqing, China	Aug 2007; Aug 2008; Nov - Dec 2009; Dec 2010
Wallace et al. 2009; Adams et al. 2012	Long-term spatial variation of air quality	An enclosed van	CO; PM_1, $PM_{2.5}$, PM_{10}; SO_2; NO, NO_2, and NO_x; GPS	Hamilton, Canada	2005 – 2010
Hagler et al. 2010; Baldauf et al. 2016	Spatial variability of near-road and on-road air pollution	All-electric converted PT Cruiser	UFP (5.6–560 nm); CO; GPS	Durham, NC, US Phoenix, AZ, US	May 2008 Oct - Nov 2013
Levy et al. 2014a, b	Multipollutant spatial variations in a large city	Diesel engine vehicle (GMC C7500 medium-duty truck)	NO, NO_2, NO_y, NO_x, NO_z; SO_2; CO; O_3, O_x; PM_{10}, $PM_{2.5}$, $PM_{1.0}$; PNC; BC; Organic matter; Sulfate; Nitrate; Hydrocarbon–like organic aerosols; Mass-to-charge ratio of 57; Benzene; C3-benzene; Toluene; Xylene; GPS	Montreal, Canada	3 weeks in winter, summer and autumn, 2009
Elen et al. 2013; Van den Bossche et al. 2015	Mapping spatial variation in urban air quality	Bicycle	UF PNC; PM_{10}, $PM_{2.5}$, $PM_{1.0}$; BC; CO; noise; GPS; temperature; RH	Antwerp, Belgium	Feb - Mar 2012
Hatzopoulou et al. 2013; Minet et al. 2018	Air pollution exposures	Bicycle, backpack	UFP (10–1000 nm) PNC; $PM_{2.5}$; BC; CO; GPS; temperature; RH	Montreal and Toronto, Canada	May, Aug 2011 May, Aug 2016
Lee et al. 2015	Particle emission of diesel vehicles; chasing	Diesel minivan (Hyundai Motor Company Grand Starex)	PNC (5.6–523 nm); CO, CO_2; NO, NO_2, NOx; THC, CH_4, nMHC; meteorology; GPS	Hwaseong, South Korea	Mar, Apr 2010
Yamada et al. 2016	In-vehicle exposure	Gasoline-powered Toyota car bB	PNC (5.6–523 nm); NO, NO_2, NO_x	Japan	4 days in 2011; 5 days in 2013, and 10 days in May 2014

Table 1 (continued)

Study	Purpose	Platform	Pollutants	Location	Time
Apte et al. 2017	High-resolution air pollution mapping	Google Street View cars	BC; NO, NO_2	Bay area, CA, US	May 2015-May 2016
Von Fischer et al. 2017; Weller et al. 2018, 2019	Detection of natural gas pipeline leaks	Google street view cars (2012 Subaru Outback Imprezas)	CH_4; GPS; meteorology	Several cities in US	2013- 2018

PSD is particle size distribution; *PNC* is particle number concentration

high degree of system integration was desired to facilitate data management and real-time assessment, e.g., allowing the vehicle to be positioned downwind, and to display trends and other results in real time to lay persons. (7) For the platform itself, we wanted sufficient space to fit the instrumentation and headroom for standing but also to keep the vehicle size relatively compact for maneuverability, easy parking, and navigating rough and tight streets, possibly with height restrictions. Step vans or trailers were considered too large. Fuel efficiency was a secondary goal. (8) We wanted the monitoring system to allow essentially automatic and unattended operation (after startup and shutdown) so that platform could be operated by the driver without a second technician. (9) Our goal was to live within a budget constraint of approximately $330,000 for new equipment, fabrication, and some software development. This excludes four instruments that we had available on-hand, which would cost ~$100,000 new (described below). (10) Lastly, we wanted the system to be built and operational within a year.

Mobile platform and configuration

Vehicle

We selected a 2018 Ford Transit truck (width, 8.12 ft., 2.47 m; length, 18.15 ft., 5.53 m; height, 8.4 ft., 2.56 m; weight, 3500 kg; fuel type, gasoline) as the platform (Figs. S1 and S2). This truck has minimally sufficient headroom for standing inside (1.8 m). A second air conditioner/heater was installed in the rear of the vehicle. We installed rigid honeycomb insulation in the interior and covered both side and rear windows to help maintain constant temperature in the vehicle. Given the amount of equipment installed, the extended length version of this vehicle would have been advantageous. In addition, as noted below, a higher vehicle would have improved access for the PM instruments, but would impose some fuel efficiency and handling penalties. We ordered upgrades for the seats and side mirrors. The vehicle is comfortable and easy to drive, the driver has excellent visibility, and the fuel economy is reasonable (about 15 mpg).

Instruments

Table 2 lists the 13 instruments selected and installed in MPAL and their measured parameters,

Table 2 Instruments deployed in MPAL

Instrument	Measured parameters	Measurement principle	No. params	Range	Resolution	Response time	Lag time
Picarro G2401	CO_2, CO, CH_4, H_2O	Cavity ring-down spectroscopy	4	CO_2: 0–5000 ppm CO: 0–1000 ppm CH_4: 0–100 ppm	CO_2: 1 ppb CO: 1 ppb CH_4: 1 ppb	2 s	26 s
Picarro G2204	CH_4, H_2S, H_2O	Cavity ring-down spectroscopy	3	CH_4: 0–100 ppm H_2S: 0–1000 ppb	CH_4: 1 ppb H_2S: 1 ppt	2 s	26 s
Eco Physics CLD 700 AL	NO_x, NO, NO_2	Chemiluminescence and UV absorption	3	NO: 0–1 ppm NO_x: 0–1 ppm	NO: 1 ppb NO_x: 1 ppb	1 s	27 s
Thermo Scientific 43iQ	SO_2	Pulsed UV fluorescence	1	0–10 ppm	0.1 ppb (e)	1 s	26 s
API 400A	Ozone (O_3)	Absorption of 254 nm UV light	1	0–100 ppb	0.1 ppb	1 s	27 s
TSI 3321	PNC, PSD (0.5 – 20.5 μm)	Time-of-flight sizing and light scattering	12	0–>10,000/cm^3	1/cm^3	1 s	4 s
TSI 3330	Particle mass concentration, PSD (0.3 – 10 μm)	Optical scattering from single particles	16	0–200 g/m^3	0.001 μg/m^3 (e)	1 s	4 s
TSI 3910	PNC, PSD (10 – 421.7 nm)	Scanning Mobility Particle Sizing (SMPS) and condensation particle counter (CPC)	16	100–1,000,000/cm^3	1/cm^3 (e)	60 s	100 s
Magee AE21 Aethalometer	BC	Filter-based, UV (370 nm) and IR (880 nm) attenuation by collected particles	2	0–>10,000 ng/m^3	100 ng/m^3	300 s	150 s
Horiba PX375	PM_{10} PM_{10} trace metals (Ti, V, Cr, Mn, Fe, Ni, Cu, Zn, As, Pb, Al, Si, S, K, Ca)	Cyclone size separation, beta-ray attenuation X-ray fluorescence	16	0–1000 μg/m^3 Measured in ng/m^3	0.1 μg/m^3	60 s 30 min	60 s (e) 900 s
Garmin 18x	location, elevation, speed, direction	Geographic positioning system (GPS)	10		15 m	1 s	1 s
Young 92000	Wind speed/direction, temperature (T), RH, atmospheric pressure	Ultrasonic wind sensor, T, RH and pressure sensors	5	WS: 0–70 m/s WD: 0–360 deg T: –40 – 60 °C RH: 0–100% P: 500 – 1100 hPa	WS: 0.01 m/s WD: 0.1 deg T: 0.1 °C RH: 0.1% P: 0.1 hPa	1 s	1 s
Spy Tec Mobius Action Camera	Front and back photos	1080P HD wide angle camera	2			2 s	

WS wind speed; *WD* wind direction; *T* temperature; *RH* relative humidity; *P* ambient pressure, (e) is estimated

measurement principle, and time resolution. Photographs are shown in Figs. S3–S5. Five instruments measure gases and five measure particulate matter (PM). A total of 11 gaseous pollutants are monitored: CO_2 (0–5000 ppm; resolution, 1 ppb); CO (0–1000 ppm; resolution, 1 ppb); CH_4 (0–100 ppm; resolution, 1 ppb; measured using two instruments); H_2O (0–100%; resolution, 0.001%); H_2S (0–1000 ppb; resolution, 1 ppt); NO, NO_x, and NO_2 (0–1 ppm; resolution, 1 ppb); SO_2 (0–10 ppm; resolution, 1 ppb); and O_3 (0–100 ppb; resolution, 0.1 ppb). PM concentrations and size distributions over a wide size range (0.01–20 μm) are measured using three instruments: an aerodynamic particle sizer (APS, TSI 3321, TSI Inc., Shoreview, MN, USA) using 12-size bins (0.5–20 μm); an optical particle sizer (OPS, TSI 3330, TSI Inc., Shoreview, MN, USA) for number concentrations in 12-size bins (0.3–10 μm) converted to mass concentrations; and a scanning mobility particle sizer (SMPS, TSI 3910, TSI Inc., Shoreview, MN, USA) for nanoparticles in 13-size bins (10–422 nm). Other PM measurements included black carbon (BC) using an aethalometer (AE21, Magee, Berkeley, CA, USA) using ultraviolet (370 nm) and infrared (880 nm) absorbance; PM_{10} using a sharp-cut-point impactor, heated inlet, and β-attenuation; and PM_{10} metals (Ti, V, Cr, Mn, Fe, Ni, Cu, Zn, As, Pb, Al, Si, S, K, Ca) using X-ray fluorescence (XRF) spectrometry. The PM_{10} and metal measurements used a new instrument (PX-375, Horiba, Kyoto, Japan) that captures PM on a PTFE/non-woven fabric membrane filter tape, which is advanced every 30 min; a separate workstation controlled this instrument. PM_{10} concentrations are determined each minute, and metals every 30 min. The Horiba PX-375 uses a sealed carbon-14 (< 10 MBq) β-ray source. The β-ray and X-ray sources in this instrument are fully shielded using thick stainless steel plates (2.6 kg), and the system includes an interlock that prevents operation if the system is opened. The University of Michigan safety staff check the system biannually to ensure radiation safety. Gravimetric PM analyses were not utilized since systems can be vibration sensitive and not suitable to a moving system, and most systems do not work with a filter tape. Potentially, a tapered element oscillating microbalance system might be adapted to provide direct measurements of particulate matter without the need for radioprotection measures, although conventional instruments require more vertical space and bench space than was available in the vehicle. The APS, NO_x, O_3, and aethalometer instruments were on-hand and utilized for MPAL after factory refurbishment.

In addition to the pollutant measurements, we obtain GPS, meteorological, and visual data. Wind direction, wind speed, temperature, relative humidity (RH), and atmospheric pressure are measured using ultrasonic and other sensors in an integrated instrument (Fig. S6, Young 92000, R.M. Young Company, Traverse City, MI, USA). Vehicle location, elevation, speed, and traveling direction data are monitored using a sensitive GPS (Garmin 18x, Garmin International Inc., Olathe, KS, USA). Both meteorological and GPS data are collected at 1 Hz. Lastly, we record time-lapse photos every 2 s from forward and rear-facing wide-angle cameras (Fig. S7; Spy Tec Mobius action cameras), which can help identify emission sources or explain unusual pollutant levels.

Sampling inlets and exhausts

Three sampling inlets were installed on the vehicle's roof (Fig. 1, Figs. S8–S11). Inlets were ~ 1 m above the roof and as far forward as possible to avoid or minimize effects of the vehicle's boundary layer while driving. (Later, field tests evaluate the representativeness of the wind measurements.) The inlet system was also designed to minimize self-pollution from the vehicle's exhaust. The inlets were roof-mounted and located ~ 3 m above and 1.7–2.5 m in front of the vehicle's tailpipe, which was located underneath and at the rear of the vehicle (~ 0.3 m above ground level and within ~ 0.3 m of the rear bumper). No evidence of self-pollution was identified during sampling. Inlet positions were constrained by locations of the truck's roof cross struts and seals and the instrument racks (described below). Gaseous samples were collected after a primary rain shield using a 2-in PVC cap that incorporated a 16-mesh stainless steel "bug" screen and a secondary rain shield consisting of a stainless steel separator within the rain cap. The sample was then drawn at 3.8 L/min into 0.25-in PTFE tubing, then through a droplet separator and PTFE filter (1 μm) to remove PM, and into a PTFE and stainless steel manifold that distributed the sample flow to five instruments (sampling at 0.4–0.8 L/min each, a total of 2.8 L/min); a small purge pump (linear) drew an additional 1 L/min as monitored and controlled by a rotameter/valve to maintain rapid flow through the

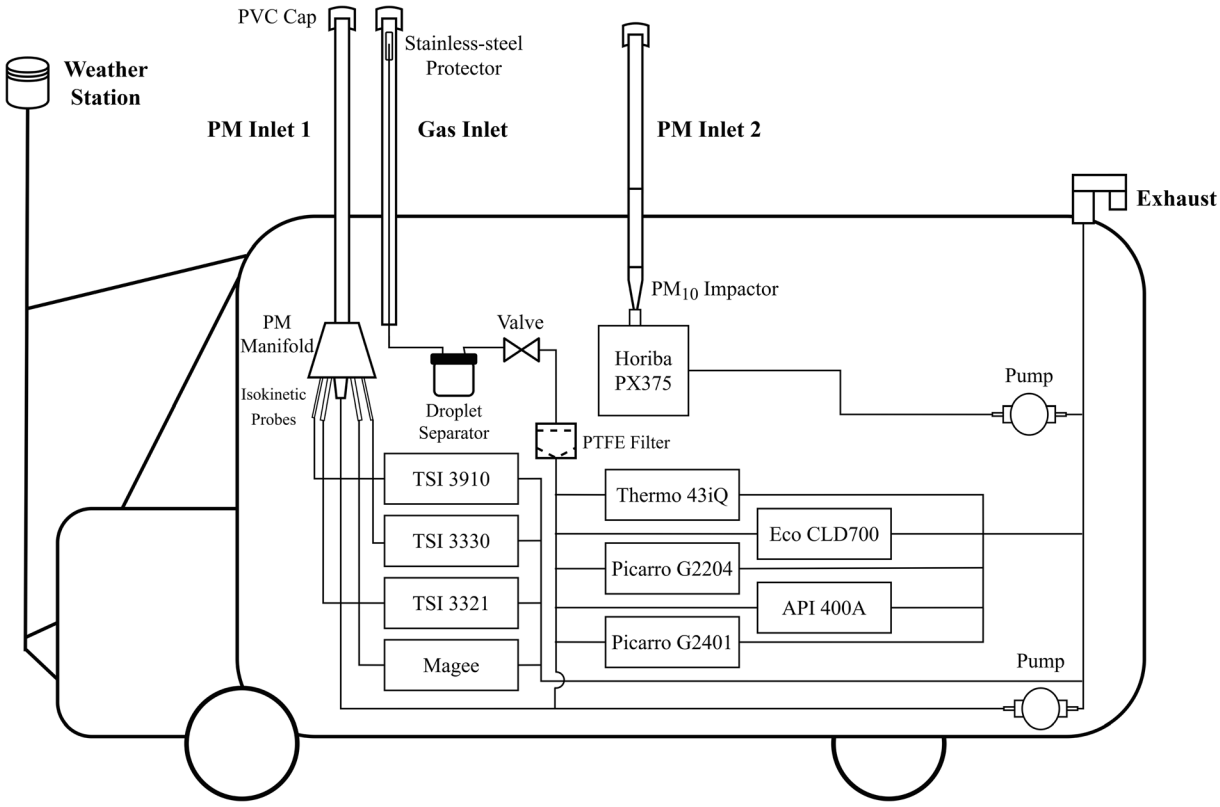

Fig. 1 Schematic of MAPL monitoring systems. Shows three sampling inlets, instrument exhaust, monitoring instruments, and weather station. Lines in the truck represent sample flow paths. GPS, power system, data acquisition system, and front- and rear-facing cameras are not shown

sampling system (Fig. S12). The total length of tubing upstream of each instrument ranged from 5.1–6.1 m. The PTFE tubing was placed inside a vertical 1-in (pipe size) PVC pipe, providing physical support, which could periscope up and be clamped in position for sampling (inlet was 0.94 m above the vehicle roof), or periscope down to minimize height and provide additional rain protection.

The two PM sampling inlets used straight tubes with tube sizes and flows selected to match instrument requirements and minimize particle losses. Both used a primary rain shield identical and could telescope up and down, also as described above. Alternative inlet and tubing designs (tubing diameter, length, transitions, and orientation) and flow rates were evaluated with the goal of minimizing PM losses in size from 0.01 to 10 μm dia using the Particle Loss Calculator (https://www.mpic.de/4128325/particle-loss-calculator-plc), which accounts for losses from diffusion, deposition, and sedimentation. Losses were highest for the largest particles (> 5 μm dia) and then the smallest particles (< 0.01 μm); the selected designs kept predicted losses below 10% in the large diameter tubing. Later, field tests are described that help confirm results and estimate overall sampling losses.

PM inlet 1 drew air directly into a clear 1-in (pipe size) PVC pipe at a flow rate of 45 L/min. In the truck, the pipe transitioned to a manifold with a four vertical probes for distributing flows to four instruments (either 0.25 or 0.125-in dia stainless or brass tubing with a knife edge). Tube diameters were selected considering each instrument's flow rate to achieve near-isokinetic sampling. Static-dissipative polyurethane tubing connected each instrument to the metal tubing. An additional purge flow of 16.5 L/min in the main sampling manifold was provided by another pump, displayed by a rotameter. The total tubing length from the inlet to the instruments ranged from 1.63 to 2.74 m.

PM inlet 2 was dedicated to the PM_{10} mass and elemental analyzer (Horiba PX375) due to its special inlet design and higher sampling rate (16.7 L/min). The probe was positioned ~ 1 m behind the gas inlet and PM

inlet 1 and ~ 0.70 m above the vehicle roof. An external pump connected to the analyzer drew ambient air into the sampling inlet and (telescoping) 0.90-m-long tube, through a short-flex coupling (needed given the shock mounting of the instruments (see below) to a heated (50 °C) PM_{10} sharp-cut impactor, into a transition tube, and then into the analyzer. The flow path (other than in the impactor) was straight and vertical and directly onto the Teflon sampling tape used by the instrument. Due to limited vertical clearance in the truck, the impactor, transition tube, and heater assemble had to be removed to the inlet and connecting tube to telescope downward into the vehicle's interior. A higher vehicle would have improved access without substantial change in PM losses; a lower rack would be disadvantageous as the Horiba PX375 instrument requires front access for loading filter tape and inspections. The straight, vertical, and relatively short sampling configuration for both PM inlets was intended to minimize particle losses (tested later).

Exhausts from the instruments were plumbed and discharged through a single weatherproof roof-mounted exhaust at the rear of the vehicle (Fig. 1). This exhaust was probably unnecessary given the normally high air change rate in the vehicle; however, it provided safety to the operator in the event of the failure of the O_3 scrubber used by the NO_x instrument.

Work on top of the truck was conducted in a high bay area using a scissor lift with a walkway extension. The larger holes in the vehicle roof (and elsewhere) were made using a hydraulic knockout punch. Despite these resources, work on the vehicle roof was awkward and physically challenging (Figs. S13 and S14).

Electrical power

A power budget was developed based on laboratory measurements of both warm-up (maximum) and operating (average) power requirements of each instrument using an in-line current meter. All instruments utilized 120 VAC power. For all instruments, the warm-up requirement totaled 1.98 kW, and the average power was 1.07 kW. Given the power needs and space and budget constraints, the power system required considerable engineering (Figs. S15–S17).

Instruments were powered by a charger/inverter (Victron MultiPlus, 12 V DC, 3 kW, 120 VAC, 120 A) that provided high-quality AC power. This unit drew from the truck's 12 V power (heavy-duty alternator plus two factory-installed 12-V lead-acid batteries mounted under the driver's seat) and five 12.8-V, 100-Ah $LiFeMnPO_4$ batteries (Prismatic, AA Portable Power Corp.), giving a total of ~ 8.8 kWh of storage. The truck's alternator was coupled to a DC-DC converter (Sterling Power BBW1260, 60 A, 12 V to 12 V) to charge the $LiFeMnPO_4$ batteries while driving, providing an additional ~ 30 A (12 V) while driving. The $LiFeMnPO_4$ batteries were equipped with a battery management system and custom designed and built voltage and current monitors to display status (e.g., drain or charge). When parked at our University of Michigan home, the $LiFeMnPO_4$ batteries were charged overnight using the charger/inverter and a 20-A 120-VAC circuit. With fully charged batteries, all instruments on and engine running, the power system supported ~ 6.5 h of continuous sampling. Much longer runs could be made by turning off high current draw instruments, e.g., NO_x and PM_{10} instruments. To reduce power needs, we used a single pump (with sufficient capacity) for the two Picarro instruments and replaced the external heated catalytic scrubber used to destroy ozone from the NO_x instrument with a carbon adsorbent (carbon was swapped out monthly). Occasionally, we were able to charge batteries during some of the (1-h long) collocation events.

The $LiFeMnPO_4$ batteries and related equipment were mounted under a bench on a low shelf (bolted to the right-side wall of the truck) and on the vehicle floor, both in front and behind the rear wheel well. The shelf was constructed of steel stock and plywood; dense foam was used to cushion the batteries. The power control and battery management system (BMS) were placed into the right wall of the truck, just above the shelf. While this allowed a relatively compact and attractive layout, fitting this hardware into the truck was challenging due to space, weight (110 kg of batteries and electronics), and access issues. In addition, this configuration required heavy cable (2/0 gauge) to minimize voltage drops between the alternator, batteries, and inverter/charger; these cables were run under the truck floor in protective tubing and in the vehicle wall to keep the floor flat. Lighter cables (6 gauge) to each $LiFeMnPO_4$ battery were run through the vehicle's wall to save space; this installation also was challenging. A long extension cord (12/3) allowed charging when parked. For electrical protection and fire safety, the connection at the vehicle's lead acid batteries were fused (150 A) and an armored cable linked this battery to the DC-DC

charger. In addition, two circuit breakers (150 A and 200 A) were installed in the BMS to protect the $LiFeMnPO_4$ batteries and inverter, and a ground fault interrupter and circuit breaker (20 A) protected the 120-V circuits. We equipped the truck with a fire extinguisher. All of the batteries were ventless types and should not off-gas.

Maintaining constant temperatures in the truck for the batteries and instruments, especially when parked, can be challenging. While equipped with a second air conditioner/heater and rigid honeycomb insulation, to avoid overheating when the engine was off, the vehicle should not be parked in direct sun on hot days for more than about an hour.

In a larger vehicle, batteries might be placed closer to the alternator or by the truck battery (under the driver's seat); additional batteries would provide longer run times; a higher voltage battery system would reduce wire size and decrease resistance losses; and 240 VAC mains would speed charging and decrease wire size. We learned not to discharge batteries excessively, which resulted in the inverter automatically shutting down; repeated shutdowns also lead to the $LiFeMnPO_4$ batteries swelling and failing. The battery management system utilized an audible alarm, but this did not always provide sufficient advance warning, e.g., a manual shutdown was not feasible while driving on highways, and several batteries were ruined prematurely.

Physical mounts and ruggedization

The system design started with the physical mounts, diagrams and weights of the racks, instruments, and truck. As described below, however, the locations of the vehicle's frame, floor ridges, roof joints, and many other details required flexibility and ingenuity. Instruments, sampling pumps, desktop workstations, and monitors were securely installed in or on top of mid-rise equipment racks (Samson SRK16 Universal Rack Stand). Shelves and drawers were installed in each rack, as were swivel wheels. We also installed a power strip and custom power monitor in each rack. We strengthened the vertical posts on most of the racks and attached mounting bolts to the suspension system. The rack's vertical posts were modified (folded inward) to provide the necessary clearance for several of the instruments.

A shock mount system was engineered to hold each rack securely, yet allow ~ 3 cm of dampened vertical movement and 1.5 cm of horizontal movement (Fig. S18). We secured three low-profile strut channels to the vehicle floor and one to the ceiling lengthwise along the truck and mounted vertical posts between racks using back-to-back channel struts separated by a gap to increase rigidity and minimize deflection in the event of a hard stop. (We calculated a maximum horizontal deflection of < 1 cm for a 2 G deceleration with fully loaded cabinets.) Then, each rack was installed using 4 or 6 (depending on equipment weight) elastomer fastener-mount compression springs (length, 2.31 in; outer diameter, 2.61 in) installed under each rack; under the heaviest rack, we also inserted bumpers (two 1-in dia solid silicon rubber tubes) for additional cushioning. Similar but smaller compression springs were used between racks to restrict and dampen horizontal movement. Space for the four racks and five vertical members was limited, and considerable fabrication was needed to meet space constraints. The system was strong but added ~ 180 kg weight (~ 100 kg for 4 racks, ~ 40 kg for struts, ~ 40 kg for associated hardware). While designed to allow rapid removal of each wheel-equipped rack, in practice, racks were never removed; thus, the wheels were unnecessary, and a simpler mounting system with potentially fewer racks could have been used.

Additional details of the mounting systems are shown in Fig. S18. Struts were mounted directly and indirectly (using brackets) to the vehicle floor and frame using through bolts, self-threading screws, and rivet nuts; floor mounting required machined risers to even out the channels on floor, and hardware needed to pass through the laminated (rubber/fabric) floor mat. Once installed, the strut channels provided great flexibility and convenience since brackets and hardware can be installed easily at most locations, although bolts that secured the low-profile strut channel sometimes interfered with the strut nuts used to mount hardware and brackets. (High-profile channels would avoid this issue but were not used due to space issues.)

The weather station and GPS instrument were mounted on the truck's exterior. The weather station was mounted on a mast at the front of the vehicle at 120 in (3.05 m) height to minimize vehicle-induced modifications of the wind flow; this location is 1.83 m above the truck's hood, and 0.7 m above and 2.2 m forward of the roof. The mount used a two-piece aluminum mast (1 in diameter, total length of 2.5 m) secured to the front bumper, and two horizontal (1 in diameter, 1.6–2 m long) tubes secured to the lower half of the mast and opposite sides of the vehicle roof/windshield pillars

to stabilize the mast. The top half of the mast, with the weather station attached, was designed to be easily removable, e.g., for parking in a garage or for access to the weather station. However, the mast was rarely removed. After about a year, the signal/power cable to the weather station connection became intermittent and required repair. The connection was replaced using a higher-quality and higher-gauge cable, routing within the mast to avoid cable movement, and eliminating a connector in the engine compartment that was prone to corrosion.

The GPS was secured to the vehicle roof. The forward- and rear-facing cameras were mounted in the truck's interior using swivel mounts: on the dashboard and in a cutout of the interior insulation at a rear window, respectively.

In addition to the shock mounting, we attempted to ruggedize each instrument, e.g., tying down tubes and wires and hardware both within the instruments and in the vehicle.

Data acquisition, onboard visualization, initial data processing

Data from each instrument (except the Horiba PX375 and cameras) were logged using an onboard desktop workstation, a serial communications hub with four USB ports and 15 RS232 ports, and a custom LabVIEW program. A wide-screen monitor was located above one of the racks; a second monitor was placed next to the driver. The LabVIEW program synchronized the instruments, interrogated each instrument, and downloaded and saved data into separate files for each instrument (Figs. S19–S23, Fig. S24 shows the Picarro software). The program's main dashboard provided a real-time display of key instrument outputs (e.g., concentrations, instrument status, errors), route driven and location, and elapsed time. Other displays selected individual instruments, displaying more parameters along with trend plots. While a large undertaking requiring ~ 5 months of programming and debugging, this program was a huge asset in facilitating data collection and management from 11 of the instruments (five monitoring gases, four monitoring PM, and two collecting GPS and meteorological data). It collected and retained 79 primary outputs from these 11 instruments, e.g., concentrations and locations, along with 60 diagnostic parameters, e.g., instrument status, flows, temperatures and pressures. Data were recorded at 1 Hz, a rate equal to or faster than the sampling frequency of each instrument. Especially older instruments can have significant latency in RS232 responses, and the program was optimized to allow data collection from each instrument, and to be fault tolerant. Potentially newer and a uniform instrument interface might be advantageous, although it would exclude certain instruments. The program also calculated, in real time, the estimated ground wind speed and direction by subtracting the GPS-determined vehicle speed and direction from the apparent wind speed and direction, respectively, measured by the onboard weather station.

Time-lapse photos were stored separately on the onboard workstation. The Horiba PX375's workstation, which ran the manufacturer's software (Figs. S25 and S26) to program the instrument, launch/terminate sampling, and schedule XRF analyses, was used to store PM_{10} and XRF data and filter tape photos.

Before and after each run, our technician/driver completed a field datasheet to record drive start/end time, instrument on/off time, pressure gauge and rotameter readings, collocation and zero check schedules, instrument zero readings, observed weather conditions, and other observations. After the run, the field datasheet was manually inputted into an Excel file and uploaded to the cloud drive, and the two onboard workstations were connected to the web via Ethernet and data similarly uploaded. Photos taken by the front and back cameras, which required considerable storage, were manually saved to a portable hard drive. A day's run generated considerable data: ~ 3.5 M data points from instruments and ~ 25,200 photos.

Performance evaluation

Instrument time response and synchronization

A series of tests were conducted to evaluate and optimize system performance before launching measurement campaigns. First, we estimated the total response time lag of each instrument, which is critical for synchronizing measurements and developing high-resolution maps. We defined the total time lag as the interval between the time the sample enters the sampling inlet to the time ~ 2/3 of the final response is reached as recorded and time-stamped by the LabVIEW program. This included the sample travel time (though the inlets and connecting tubing), instrument processing time, and instrument-to-LabVIEW communication time. These times were determined using step changes in test atmospheres (e.g., introducing gases or scrubbing/filtering air), both with and without tubing and

inlets. Total lag times ranged from 4 s (TSI instruments) to 900 s (Horiba PX375).

PM sampling system losses while stationary

Performance characteristic of a PM sampling system depends on many factors, including the inlet efficiency, losses within tubing (e.g., diffusion, deposition, and sedimentation), sizing characteristics of the instrument (e.g., cutpoints and penetration curves), particle characteristics (e.g., shape, size, density), and environmental conditions (e.g., wind speed, humidity). The following sections describe experiments conducted that consider losses under stationary (negligible wind velocity) and moving conditions.

Two sets of experiments were conducted to help confirm the particle loss calculations used in the design of the PM sampling system and to provide overall estimates of particle losses in the inlet and tubing; results of these experiments are extended in moving tests (described in the next section). The first set was conducted while the vehicle was parked in a large garage, and the three TSI instruments in MPAL and two new handheld optical particle counters (OPCs) that provided simultaneous and continuous 1-min measurements of PM_1, $PM_{2.5}$, and PM_{10} (Aerocet 531 s, Met One Instruments Inc., Grants Pass, OR, USA) were used. A short (0.3 m) length of tubing was connected to each Aerocet OPC as an inlet throughout the tests. One OPC was used as a reference; the second was periodically collocated with the reference instrument (e.g., before and after each test period) to check responses (which were very similar).

The first experiment evaluated overall PM losses (including the inlet, large- and small-diameter tubing) by comparing measurements obtained under two configurations: the "collocation" configuration operated the three TSI instruments inside MPAL with doors open with no tubing attached and the two Aerocet OPCs on the roof of MPAL near PM inlet 1; and the "test" configuration operated the TSI instruments connected to PM inlet 1 using their usual tubing, the test OPC was placed in the truck and connected to the PM inlet 1 using a spare isokinetic probe (like the TSIs), and the reference OPC remained on the MPAL roof. This experiment had five phases, sequentially obtaining collocation, test, collocation, test, and collocation measurements. Each phase collected at least 5 min of data.

Size-specific particle losses $L_{0,TSI,D}$ (%) were calculated for each TSI instrument and each experiment as:

$$L_{0,TSI,D} = \left[\left(1 - C_{TSI,TEST,D}/C_{TSI,COL,D}\right)\right] \times 100\% \quad (1)$$

where $C_{TSI,TEST,D}$ and $C_{TEST,COL,D}$ = average concentrations for size range D measured during test and collocation configurations, respectively, for one of the TSI instruments. Concentrations in each particle size range were obtained by differencing size channels (e.g., $PM_{1–2.5}$ was obtained by subtracting PM_1 from $PM_{2.5}$ measurements). The second collocation period was weighted twice. Time windows to determine concentrations $C_{TEST,D}$ and $C_{COL,D}$ were determined by reviewing trend plots to ensure stationary measurements (most windows contained the entire 5-min period). In the case of the Aerocet OPCs, the test OPC was first calibrated to match the reference OPC using regression, and then losses ($L_{0,Aerocet,D}$) were calculated using Eq. (1) with the calibrated concentrations (Refer to the SI for details.). Uncertainties of these tests were estimated through error propagation. (Refer to the SI for details.)

The second experiment estimated PM losses through the small-diameter tubing (including isokinetic probes and flexible tubing). Isokinetic probes for the TSI instruments were detached from the manifold and placed near each other and near the two inlets of the two Aerocet OPCs, which were located in MPAL near the TSI instruments throughout the experiment. Again, two configurations were used. In the "collocation" configuration, all instruments were run without the inlet tubing attached. In the "test" configuration, the three TSI instruments and one Aerocet OPC were operated attached to their respective small-diameter tubing, and the reference Aerocet OPC was operated without the inlet tubing as before. Again, five sequential phases were used, as described above for the overall loss experiment.

Overall inlet losses were estimated for submicron particles at five size ranges (10–42, 42–75, 75–133, 133–237, 237–422 nm) using the TSI 3910, and for micron-sized particles in five size ranges (0.3–1, 1–2.5, 2.5–4, 4–6, 6–10 μm) using data from the TSI 3321, TSI 3330, and Aerocet instruments.

PM sampling system losses while moving

PM losses in sampling inlets depend on wind speed. For mobile platforms, driving speed and wind velocity can become important. Wind tunnel tests of inlet performance

for a large vehicle like MPAL are not practical and would not reflect effects of nearby vehicles and obstacles that can induce boundary layer effects and flow disturbances. Instead, we utilize two field campaigns in which measurements while driving at 15–45 mph (7–20 m/s) are compared to "baseline" measurements obtained while stopped immediately before and after the driving tests, ideally in an area and time when PM levels are constant. We considered several sufficiently long (e.g., > 5 km) and flat paved roads that allowed a range of speeds (i.e., minimal traffic and posted speed limit of 50 mph) in areas without known PM sources, or with little heterogeneity in local sources.

A pilot campaign was conducted in Michigan in a nearby largely rural area. These tests identified the need for longer-duration baseline measurements and, post hoc, some interfering PM sources were identified (e.g., fugitive dust at intersections with unpaved roads). The final campaign was performed on an 8.4-km-long and flat section of a road located 1.2 km north and parallel to Interstate 90 (I-90) in northeastern Ohio (Country Road J between Route 20 and 108), a rural area with no known local PM sources other than very occasional traffic on unpaved crossroads (tractors and some personal vehicles). We avoided periods when fugitive dust from agricultural operations or pollen was present. I-90 has considerable car and truck traffic: the annual average daily traffic (AADT) volume is 63,797 vehicles/day and the commercial traffic (CAADT) is 6851 trucks/day, most of which are heavy-duty diesel vehicles (Ohio Department of Transportation 2018). There are no exits or ramps to I-90 in this area and traffic speed tends to be very constant on this straight and flat and highway segment.

Each test at a given speed had five phases: (1) "baseline" PM levels were measured for 5 min while parked at one end of the road section; (2) "moving" PM levels were measured while driving to the other end of the road section at the selected speed; (3) baseline levels were again measured while parked for 5 min at the other end of the road section; (4) moving PM levels were again measured while driving back (in the opposite direction) to the starting location; and finally (5) baseline levels were measured for a third time while parked. These tests were conducted at four driving speeds and involved two technicians to operate the vehicle and to track and document activities. After excluding transition periods, we took the median concentrations in each parking and driving phase, from which we calculated the average baseline concentration $C_{0,D}$ (weighting the 2nd baseline measurement twice) and the average driving concentrations $C_{V,D}$ at the specific speed V (m/s) and particle size range D (μm in diameter). We then estimated speed- and size-specific inlet sampling losses $L_{TEST,V,D}$ acquired in the test as:

$$L_{TEST,V,D} = \left[1 - C_{V,D}/C_{0,D}\right] \times 100\% \quad (2)$$

Time windows to determine concentrations $C_{V,D}$ and $C_{0,D}$ were selected considering the vehicle speed and trend plots of PM concentrations. We excluded ~ 40 s in the beginning and end of each phase to allow the vehicle to reach the desired speed and several periods when PM levels were non-stationary. The baseline periods averaged 260 s in duration; moving periods ranged from 260 to 980 s in duration, depending on the driving speed. We estimated standard deviations for $C_{0,D}$ and $C_{V,D}$ and calculated the uncertainty of $L_{TEST,V,D}$ through propagation of error analysis. Because two of the instruments used for this analysis (TSI 3321 and TSI 3330) obtained 1-s measurements, and because the median concentrations were used, results of this analysis are robust. During the field tests, winds were light (1.8 m/s) southerly winds and low relative to vehicle speeds (7–20 m/s); also, the apparent wind speed measured by the MPAL sensor was within 0.2 m/s of vehicle speed. Estimates of $L_{TEST,V,D}$ were plotted against the apparent wind speed V_w as measured by the weather station (accounting for vehicle speed and wind speed) and, where appropriate, fitted regression lines to the data or estimated an average loss. These analyses were performed for the five submicron and the five micron particle size ranges described earlier.

The total particle loss is the product of the stationary inlet loss ($L_{0,D}$ from Eq. 1) and the moving loss ($L_{V,D}$ as discussed in this section); thus, PM concentrations were corrected by the following equation:

$$C_{COR,D} = C_{RAW,D}/\left[\left(1 - L_{0,D}\right) \times \left(1 - L_{V,D}\right)\right] \quad (3)$$

where $C_{COR,D}$ and $C_{RAW,D}$ are the corrected and raw concentrations of particles in size range D, respectively.

Accuracy of wind measurement

Measurements of wind speed and direction from MPAL's onboard weather station can be affected by turbulence and boundary layer effects from MPAL itself, nearby vehicles (e.g., passing trucks), and atmospheric conditions (e.g., wind velocity, direction, atmospheric stability). We contrasted vehicle speed (from MPAL's GPS) and apparent wind speed and direction (from the onboard weather station) using data collected at high vehicle speed on

highways, low speed on local streets, and when stopped. These evaluations were performed on four mornings that had a range of wind speeds (1.6–5.5 m/s) as measured at three local airports. Using 1-s measurements, we calculated the wind velocity residual as ΔU = vehicle speed – wind speed, and the wind direction residual as ΔD = the absolute value of raw wind direction (corrected for quadrant shifts exceeding 180°). ΔD indicates the shift in wind direction relative to the vehicle's forward direction (with current weather station setup, the vehicle direction is 180° constant and wind from forward of the vehicle is 0° constant). To investigate possible effects of local traffic and vehicles, ΔU was plotted against simultaneously measured NO_x, CO, and CO_2 concentrations, which are indicators of traffic volume. To investigate the effects of turbulence in front of the vehicle, ΔD was plotted against ΔU; large deviations from zero suggest the influence of turbulence on wind measurements.

Quality assurance and maintenance

Zero checks were conducted weekly, usually before or after collocation (described below). These checks used a 20-L Tedlar gas sampling bag filled with zero air (~ 80% N_2, ~ 20% O_2) connected to the gas sampling inlet and an extended surface area 1 μm pore size filter connected to the PM sampling manifold. Times and instrument readings after stabilization (after 5–15 min) were documented on the field sampling datasheet.

Collocations in which MPAL was parked next to a monitoring site operated by the Michigan Department of Environment, Energy, and Great Lakes (EGLE) were performed weekly during field campaigns. To avoid self-pollution from the vehicle's exhaust, the vehicle was positioned facing upwind, or the vehicle's engine was turned off if battery power was sufficient to support the day's sampling. Because EGLE maintained data as hourly averages, collocations were scheduled at the start of the hour and lasted for at least 45 min.

Instrument and system maintenance followed manufacturer's protocols and our standard operating protocols (SOPs). Seasonally or after ~ 50 days of sampling, we calibrated the NO_x, SO_2, and O_3 instruments using a dynamic diluter and certified zero and span gases, and the CO instrument (Picarro G2401) was checked with zero and span gases at the EGLE instrument shop in Lansing, Michigan. The TSI instruments were sent back for calibration after a year's operation. Generally, the Magee aethalometer does not require calibration, though flows were regularly checked, and the instrument was collocated with other aethalometers for extended periods (several days). For the Horiba PX375, we checked the X-ray intensity and energy calibration every 6 months. The Picarro G2401 and G2204 were checked using CH_4 and H_2S standards. In addition, CH_4 is measured independently by these instruments, and the zero check and typical atmospheric levels (2.0 ppm) represent additional quality checks.

Preliminary data validation and consolidation

Initially, the raw (e.g., 1-s) data were reviewed and consolidated using a set of Excel workbooks and macros. These incorporated calibrations, the total lag time of each instrument, and checks that sample flows, temperatures, sampling and reactor pressures, and concentration readings were in acceptable ranges. After this review step, 5-s block averages were calculated if at least 3 of 5 1-s observations in the block were valid, and 60-s averages were calculated if at least 45 of 60 1-s observations were valid. The same steps were used to validate data from the TSI 3910, Magee aethalometer, and Horiba PX375 instrument, except that data were exported with their original time resolution. The validated and averaged gaseous, PM, and GPS/meteorology data were consolidated by day for a second review and then consolidated across days for use in statistical and mapping analyses. Horiba PX375 data were not presented in this article but will be included in our future publications.

Application

Study region

Mobile monitoring focused on a 17 × 10 km area in southwest Detroit that contained a range of emission sources, including heavy industry, construction, and transportation sources, which were interspersed among residential areas (Fig. 2). The nearby industrial sources include several coal-fired power plants, a petroleum refinery (capacity of 132,000 barrels per day), two steel mills and a coking plant, a truck assembly plant, gypsum and cement production facilities, a large waste water treatment plant, and many intermodal and logistics hubs, including multiple rail lines and ships at the Port of Detroit. The study area includes a US-Canada border that 9000 heavy-duty trucks cross daily; many of these trucks use surface streets in Detroit. Construction activities related to the Gordie Howe

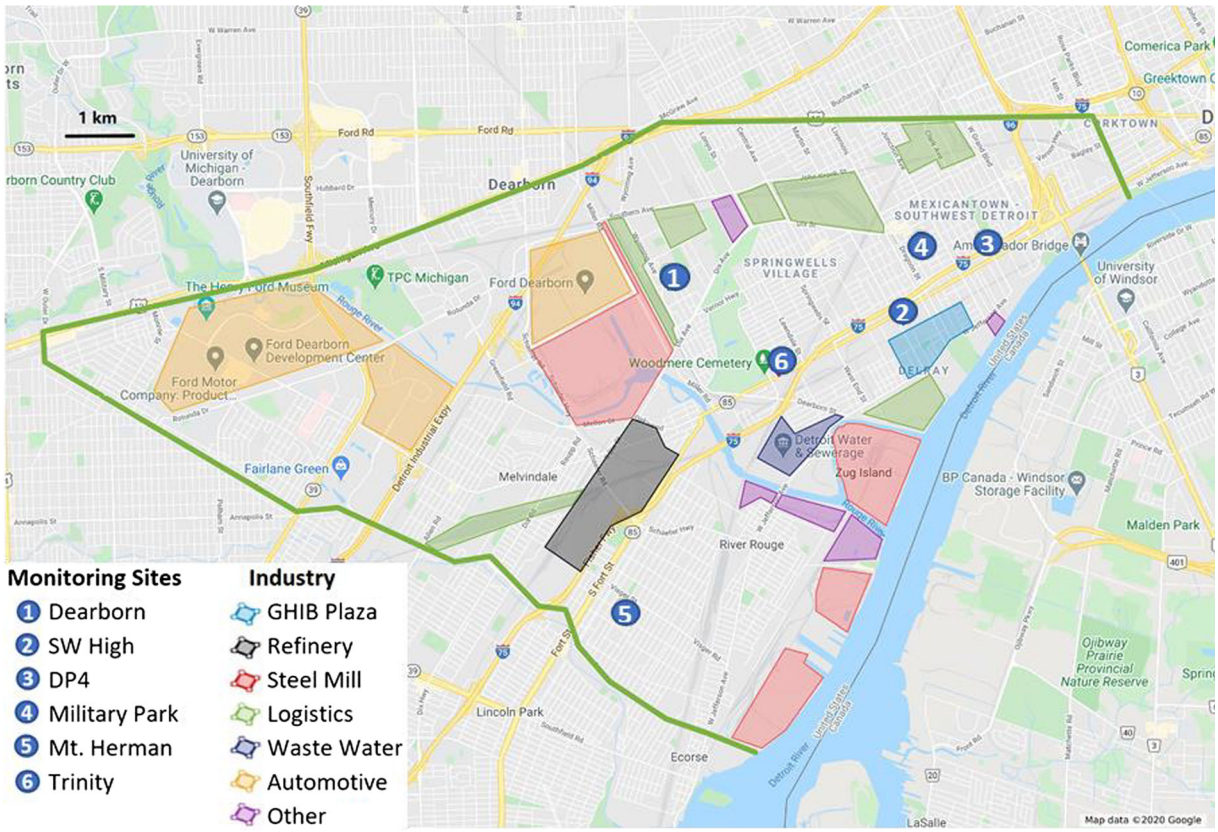

Fig. 2 Map of the study area in Southwest Detroit. Green lines indicate sampling region boundaries

International Bridge (GHIB) (starting in late 2018 with completion anticipated in 2024), including land and structure clearing, reconstruction of ramps and highways, and constructing of a new bridge across the Detroit River and a large customs/immigration plaza, represent additional emission sources.

Data collection procedures

Mobile monitoring was conducted in the study area from March 28, 2019 to March 18, 2020, typically on two days per week (total of 84 days). On most days, MPAL was not driven on fixed routes; instead, a daily route map was generated and reviewed to ensure comprehensive and repeated sampling in the entire region. Typical runs required 5–7 h, depending on the battery charging condition and driving mode. Three sampling periods (6:30 am–1:00 pm; 9:00 am–3:30 pm; 2:00 pm–8:30 pm) captured morning and evening rush hours, as well as daytime periods with ongoing GHIB construction. Most runs included a high-speed (65 mph = 105 km/h) commute from Ann Arbor (where MPAL was parked and maintained) to Detroit some 80-km distant, low-speed sampling (< 15 mph = 24 km/h) on residential roads in the study area, and moderate speed sampling (< 25 mph = 40 km/h) on larger roads in the study area. QA and collocations were performed weekly at EGLE sites in Southwest Detroit (described earlier).

Results and discussion

Wind speed and direction accuracy

Differences between apparent and actual vehicle speeds are summarized in Table 3. On neighborhood streets, speeds averaged 5.6 m/s, including frequent stops at intersections. Data were grouped into stopped and driving (> 3 m/s) conditions. While driving, the apparent wind and vehicle speeds matched closely ($\Delta U = -0.3 \pm 2.5$ m/s (average ± standard deviation) and wind directions were measured reasonably accurately ($\Delta D = 15.7 \pm 24.5^{o}$) (Figs. S27–S28). ΔD was elevated largely due to sampling on 03/06/2020 when wind speeds at the three local airports

Table 3 Summary of wind velocity residuals (ΔU), wind direction residuals (ΔD), and NO_x, CO and CO_2 concentration averages on highways, local streets, and while stopped on local streets. Data collected on four spring days (4/24/2019, 5/15/2019, 2/12/2020, 3/6/2020). *Speed occasionally dropped to <6 m/s during congestion

Type	Parameter	Highway* (>15 m/s)	Local Street-Driving (>3 m/s)	Local Street-Stopped (<0.01 m/s)
Surface Meteorology	Wind speed average (m/s)	3.0	3.6	3.6
	Temperature average (°C)	5.2	7.0	7.0
Vehicle Speed	Average (m/s)	27.2	5.6	0.0
	Range (m/s)	15–35*	3–18	<0.01
ΔU (m/s)	Average	4.1	0.3	–2.3
	Stdev	2.1	2.5	1.4
	Median	3.9	0.6	–2.3
	Max	11.3	6.8	0.0
ΔD (°)	Average	3.1	15.7	69.1
	Stdev	2.2	24.5	47.0
	Median	2.7	7.0	59.1
	Max	17.6	173.5	174.6
Pollutant concentation	NO_x (ppb)	108	62	64
	CO (ppb)	639	318	289
	CO_2 (ppm)	492	438	442

*Speed dropped to 0 – 6 m/s during congestion

were relatively high (5.5 m/s) and similar to the average vehicle speed (5.1 m/s). When stopped, ΔU is the wind speed measured at the vehicle (averaging 2.3 ± 1.4 m/s), and ΔD is the difference between the wind direction and MPAL's orientation. These results indicate that the far forward and elevated location of MPAL's weather station minimized vehicle-induced artifacts while driving at low to moderate speeds. The results also indicate a moderate degree of sheltering by trees and buildings in the largely residential and commercial neighborhoods.

On limited access highways, several effects were associated with speed, traffic and congestion, and atmospheric conditions. In free-flowing traffic (vehicle speed > 15 m/s, average of 27.2 ± 3.8 m/s), the apparent wind speed showed a modest decrease from vehicle speed (ΔU = 4.1 ± 2.1 m/s), but wind direction matched the vehicle direction (ΔD = 3.1 ± 2.2°). Congestion on the highway occasionally reduced the vehicle speed to a standstill. In congestion (vehicle speed < 15 m/s), apparent and vehicle speed and direction diverged somewhat (ΔU = 1.5 ± 2.0 m/s; ΔD = 15.6 ± 29.9°). The stop-motion photographs showed that cars in front of or passing MPAL did not affect measured wind speed or direction. However, when following trucks within 30 m at high speeds (26.7 ± 0.7 m/s), the apparent wind speed decreased (ΔU = 6.7 ± 2.5 m/s, maximum of 13.5 m/s), and NO_x, CO, and CO_2 concentrations became elevated, suggesting wake and cavity effects (Figs. S29–S30). We also found that ΔU increased during likely nocturnal inversions (based on meteorological and pollutant information), e.g., ΔU increased to 5.0 ± 2.4 m/s during an early morning drive (vehicle speed of 25.7 ± 7.6 m/s) on May 15, 2019. Additional micrometeorological data (e.g., temperature profiles) are needed to confirm these speculations. We found weak correlation between ΔU and concentrations of traffic-related pollutants (NO_x, CO, CO_2) on highways, and near-zero correlation on local streets (Figs. S31–S32), suggesting pollutant concentrations alone are not consistent indicators of wind field disturbance.

Overall, MPAL's weather station provided reasonably accurate and unbiased wind velocity and direction measurements at lower vehicle speeds (< 15 m/s); thus, differencing the vehicle and apparent wind velocity vectors would yield accurate estimates of surface winds and plume directions. At higher speeds, wind speed biases were modest to moderate, particularly when closely following large vehicles.

On-road exposure

Differences between concentrations on highways and local streets are shown in Table 3, which compares

measurements at similar times of day (early morning) on 4 days (examined above for ΔU and ΔD). On the highway, NO_x, CO, and CO_2 levels were elevated by 74%, 101%, and 12%, respectively, compared to local streets. On local streets, concentrations while moving or stopping were similar. The elevated concentrations on highways primarily reflect the emissions from the greater density of vehicles on the busy roads, higher emission rates due to the power requirements at speed, and a different vehicle mix, e.g., more trucks; they may also reflect differences in dispersion characteristics, e.g., faster winds and increased turbulence on the highway as compared to sheltered residential areas, and a weakening and disappearance of the nocturnal inversion. Pollutant levels in residential neighborhoods likely reflect "background" levels or the "urban plume."

PM losses in the sampling system

Experimentally determined PM sampling losses during stationary sampling are summarized in Fig. 3A. As expected, losses depended strongly on particle size: losses for the smallest (10–42 nm dia) particles approached 50%, decreased to < 5% for 1–3 μm particles, and then increased to nearly 70% for 10 μm particles. Results for 1–10 μm dia particles measured by the three separate instruments (TSI 3321, TSI 3330, and Aerocet OPC) were similar, although the TSI 3330 and 3321 instruments had large uncertainties (these instruments provided 1-s averages). Uncertainties were smaller for the Aerocet OPCs, due to the 1-min sampling rate and the use of two instruments that better controlled for possible concentration changes over the sampling period. All instruments showed large uncertainties for large particles due to the relatively low and variable concentrations experienced over the sampling period. Figure 3B combines results from the three instruments, showing total losses for 10 nm to 10 μm dia particles. These results reflect total system losses (including inlet and connecting tubing). Experiments quantifying particle losses in the small tubes (a subset of sampling the system loss) are summarized in Fig. S33. Again, the three instruments obtained similar results, which showed slightly smaller losses than the total system losses, as expected. The most significant losses occurred for the smallest particles (38% for 10–42 nm dia particles) and the largest particles (22–70% for 4–10 μm dia particles). The small tubing losses represent most (50–96%) of the total system losses.

In summary, experimental results during stationary sampling show inlet losses below 10% for particles from 42 nm to 2.5 μm in dia. As suggested by the simulations used to design the system, larger particles (6–10 μm dia) had losses due to inertial and turbulent impaction and settling, while very small particles (< 40 nm dia) were lost mostly due to diffusional deposition. Losses could be reduced by shortening and straightening the tubing connecting the instruments to the isokinetic manifold, eliminating the isokinetic manifold and potentially repositioning instruments directly beneath the sampling inlet (as done for the Horiba PX375). However, this was not possible given MPAL's compact configuration and the desire to utilize multiple instruments within the sampling manifold. Overall, these results suggest that the design of the sampling system provided acceptable results for gravimetric $PM_{2.5}$ measurements since particles below ~ 50 nm dia represents a very small fraction of $PM_{2.5}$ mass.

Effect of wind speed on PM losses

Inlet losses of PM while moving at velocities up to 20 m/s are displayed in Fig. 4. Particle losses are estimated separately for the TSI 3330 data (mass concentration) and TSI 3321 data (number concentration) after binning outputs into four particle size ranges. Piecewise lines in the figure were fitted to overall trends, as discussed below. For particles under 1 μm dia, wind speed had little effect, e.g., PM_1 losses ranged from 0.3 to 3.0%. For particles exceeding 1 μm dia, losses increased with particle size and vehicle velocity and reached a maximum of 56% for $PM_{4–10}$ at a wind speed of 20.4 m/s (45 mph). After testing several alternative formulations, we fitted linear trend lines through the origin (U = 0 m/s) to match the data; however, these lines are uncertain for a number of reasons. Variability increased for the largest particles, which were measured at low concentrations during the tests, which increased uncertainties, especially for $PM_{4–10}$, although the two instruments showed similar results. During the ~ 6-h period needed to collect the field data, ambient PM levels were constant for most experimental phases (stationary and moving; see examples in Fig. S34), and winds were light (averaged 1.8 m/s, maximum < 3 m/s); thus, vehicle speed was similar to apparent wind speed, supporting the validity of the tests. Only four wind velocities were tested, and we had no data below < 7 m/s. For $PM_{1–2.5}$, the linear model through the origin fitted all of the data relatively closely ($R^2 = 0.64$). For the larger size fractions, the fit was

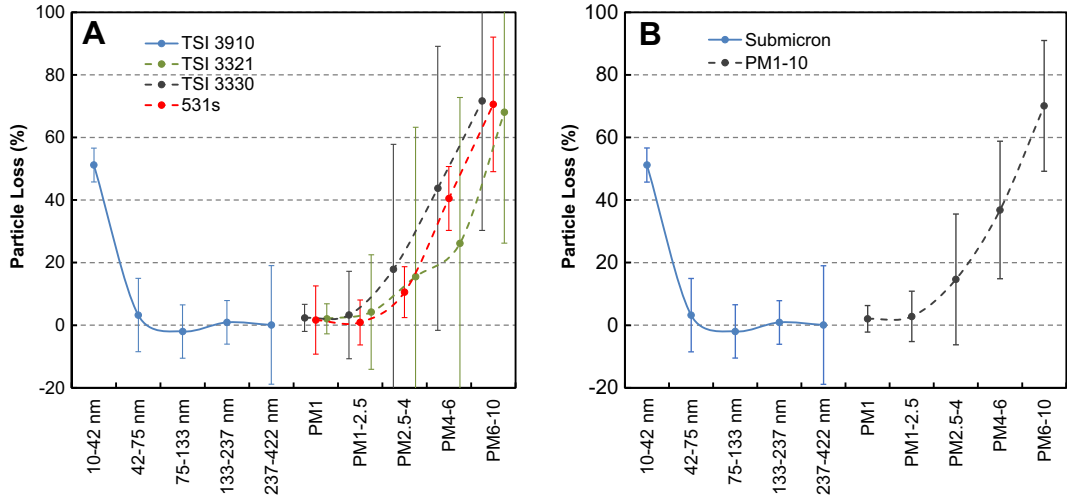

Fig. 3 (A) Overall PM inlet loss estimated using the three TSI and two Aerocet 531 instruments. (B) Consolidated PM loss estimates

reasonable at low wind velocities ($R^2 = 0.50$–0.83); a plateau was seen at higher velocities, e.g., $PM_{4–10}$ losses of 50% for wind velocities from 11 to 21 m/s. Using the bilinear models, the estimated PM losses at four wind speeds are listed in Table 4.

The bilinear model was used to adjust the PM_1 and $PM_{1–2.5}$ concentrations (measured by TSI 3330 and 3321 instruments). Considering data collected in the Detroit study area (mostly at lower speeds), the inlet and wind speed adjustments increased $PM_{2.5}$ by 7%. Due to uncertainties, $PM_{2.5–10}$ concentrations were not adjusted. (Coarse mode PM sampling losses will be examined in future research.)

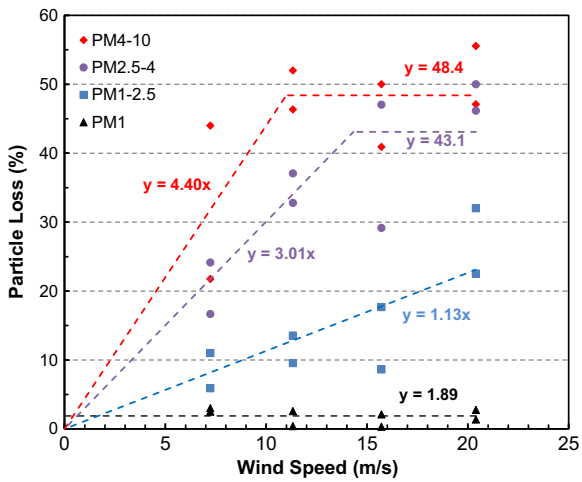

Fig. 4 Estimated particle loss versus apparent wind speed. Selected particle size ranges were analyzed together for TSI 3330 and TSI 3321. Based on tests conducted on a 5.2-mile-long section of a paved road in a rural area 0.75 mile north of highway I-90 on August 12, 2019

MPAL's measurements of PM_{10} (Horiba PX375) and BC (Magee AE21) include PM over a range of particle sizes. Because these instruments collect 1 to 30-min measurements, results were more variable than those obtained by the TSI instruments, which collected 1-s measurements. In most cases, BC results will be dominated by particles in approximately 0.3–2.0 μm dia size range, based on the particle distributions observed during the tests, suggesting that sampling losses for larger particles may not be consequential. For BC, we observed ~5% losses for vehicle speeds below 11.3 m/s, and ~10% losses at vehicle speeds above 15 m/s. These results have relatively large uncertainties, and further investigation with longer (> 15 min) stationary and moving phases appears warranted. PM_{10} measurements by the Horiba PX375 did not yield useful estimates of inlet losses, probably due to the long lag time. Since PM inlets 1 and 2 were identical and similarly placed, we expect comparable results. (The Horiba PX375 data will be discussed in a future publication.)

Data completeness and comparability

Data collected during the initial year of operation, which included runs on 84 days from March 28, 2019 to March 18, 2020, is summarized in Table 5. The dataset was consolidated into 5-s average observations (N = 376,415), most of which were collected in the study region shown in Fig. 2 (N = 265,816, excluding collocations and zero checks). An example of validated, 5-s data for one sampling day (01/10/20) is shown in Fig. S35; the corresponding driving route is shown in Fig. S36.

Table 4 Summary of estimated PM losses (in %) for PM_1 and PM_1-$PM_{2.5}$

PM Size	Wind Speed (m/s)	Inlet Loss (%)	Loss due to Driving (%)	Total Loss (%)
PM_1	All speeds	2.0	1.9	3.9
PM_1–$PM_{2.5}$	0	2.8	0.0	2.8
	7	2.8	7.9	10.5
	12	2.8	13.6	16.0
	25	2.8	28.3	30.3

Inlet and PM_1 losses are constant. PM_1–$PM_{2.5}$ losses increase with apparent wind speed

Data completeness over the study period exceeded 90% for most instruments. Exceptions included the Picarro G2204, which was returned to the manufacturer for repair (June–August, 2019), which as a result reported only 78% valid CH_4 data and 50% valid H_2S data (28% of H_2S measurements were negative and removed); the Thermo Scientific 43iQ had a sensor connector fail and calibration problems (in June and July 2019), resulting in 33% completeness, and the aethalometer (84–86%) due to its lag in response time (one or two data points were missing at the end of each sampling day since data were not completely generated before stopping the LabVIEW program). Most (85%) measurements in the study region were collected between 9 am and 5 pm; however, 3.4% were obtained during morning rush hour (7–9 am) and 9.5% during evening rush hour (5–7 pm). Most (87%) measurements in the study area were obtained on local streets with vehicle speeds below 10 m/s (22.3 mph; Fig. 5); however, 2.8% were acquired at speeds above 15 m/s (34 mph). 32.9% of the data were acquired when the vehicle was stopped (< 0.01 m/s).

Pollutant concentrations in the study area (Table 5) were compared with averaged measurements collected at 2–7 EGLE sites (depending on the data availability) in Detroit for the periods corresponding to sampling. Average concentrations measured by MPAL for O_3 and CO (26 ppb and 265 ppb, respectively) were within 20% of the EGLE data (33 ppb and 274 ppb). We measured NO_x (31 ppb) and BC (1003–1044 ng/m^3) levels that were 23–31% higher than the EGLE measurements (25 ppb and 795 ng/m^3), reflecting MPAL's on-road measurements of these traffic-related pollutants. Adjusted $PM_{2.5}$ concentrations (TSI 3330) averaged 7.1 μg/m^3, slightly below the EGLE's average (9.8 μg/m^3, data collected on seven sites). Further experiments and analyses of PM_{10} loss might increase corrected values. Our average SO_2 concentration (0.9 ppb) was 46% lower than the stationary measurement (1.6 ppb); however, several of the EGLE sites were at SO_2 "hotspots" and levels outside these areas tend to be very low. We measured an average CO_2 concentration of 419 ppm, slightly above the 415-ppm monthly average atmospheric CO_2 concentration; (Monthly Average Mauna Loa CO2 2020) as noted, traffic emissions may elevate CO_2. The Picarro G2204 and G2401 detected average CH_4 concentrations (2.05–2.06 ppm) that were comparable to the 1.9 ppm global average for 2020 reported by the NOAA Global Monitoring Laboratory (Global CH_4 monthly means 2020). CH_4 peaks were detected at several locations within the study area, likely due to natural gas pipeline leaks. The peaks were typically 20–40 s in duration (or 100–200 m wide along the driving route), and the maximum concentrations were 34 ppm and 70 ppm as measured by the Picarro G2204 and G2401 instruments, respectively. We noticed differences in peak concentrations reported by the two Picarro instruments (to be reported on elsewhere). Occasionally, unreasonable concentrations are reported for pollutants. For example, Table 5 shows that the minimum O_3, NO, H_2S, CO, and SO_2 concentrations were negative, and the minimum and maximum levels of CO_2 (311 ppm and 1316 ppm) appear unlikely. These outliers are likely errors that can result from several sources, e.g., measurements near the instrument's detection limits, very rapid concentration changes, or physical disturbances (after a big bump). These outliers are generally infrequently and mostly short-lived (1–20 s in duration), and improved algorithms to filter out events will be used in future data processing.

Conclusions and future applications

This article discussed the development and evaluation of a mobile platform for air quality monitoring. The Michigan Pollution Assessment Laboratory (MPAL) includes 13 instruments (five instruments monitoring gases, five measuring PM, GPS, weather station, and front

Table 5 Summary of 5-s data collected on 84 days (March 28, 2019-March 18, 2020)

Pollutant	Valid Sample size	Completeness	Average	Standard Deviation	Min	25th Percentile	Median	75th Percentile	98th Percentile	Max	Unit
O_3	261144	98%	26.4	12.1	–4.5	18.1	25.8	33.5	54.1	75.2	ppb
NO	242602	91%	11.0	19.0	–8.6	2.6	5.6	11.4	67.6	296.4	ppb
NO_2	239064	90%	19.8	14.8	0.0	10.8	16.2	23.4	69.8	231.0	ppb
CH_4_G2204	206029	78%	2.1	0.3	1.9	2.0	2.0	2.1	2.4	33.8	ppm
CH_4_G2401	255971	96%	2.1	0.5	1.7	2.0	2.0	2.1	2.4	69.6	ppm
H_2S	133371	50%	4.0	3.1	–0.1	1.9	3.5	5.5	11.1	237.0	ppb
CO_2	255972	96%	419.3	31.8	311.5	405.8	419.2	428.2	461.5	1316.0	ppm
CO	253243	95%	264.7	265.5	–9.0	165.4	208.6	283.0	838.6	25199.6	ppb
SO_2	86449	33%	0.9	2.0	–0.2	0.1	0.4	0.8	6.0	29.9	ppb
$PNC_{3.0}$_Corrected_TSI3321	245121	92%	1899.1	8104.6	14.6	153.4	369.6	867.6	28941.4	75155.0	#/cm^3
PNC_{10}_TSI3321	256464	96%	1788.3	7637.2	13.8	155.4	370.6	840.2	24771.5	68871.8	#/cm^3
$PM_{2.5}$_Corrected_TSI3330	251710	95%	7.1	11.2	0.2	2.8	4.8	8.6	27.4	686.0	µg/m^3
PM_{10}_TSI3330	263052	99%	35.4	101.4	0.3	10.0	18.4	33.4	193.8	11656.5	µg/m^3
$PNC_{0.1}$	21024	95%	14442.5	17051.7	745.0	6025.5	9730.7	16524.1	59030.4	311779.1	#/cm^3
BC370nm	3793	86%	1002.6	1370.5	0.0	460.0	728.0	1187.0	3472.5	44368.0	ng/m^3
BC880nm	3736	84%	1044.1	1220.8	2.0	428.0	740.0	1246.3	4038.0	19438.0	ng/m^3

Total observations N = 376,415; valid observations in the study region = 265,816

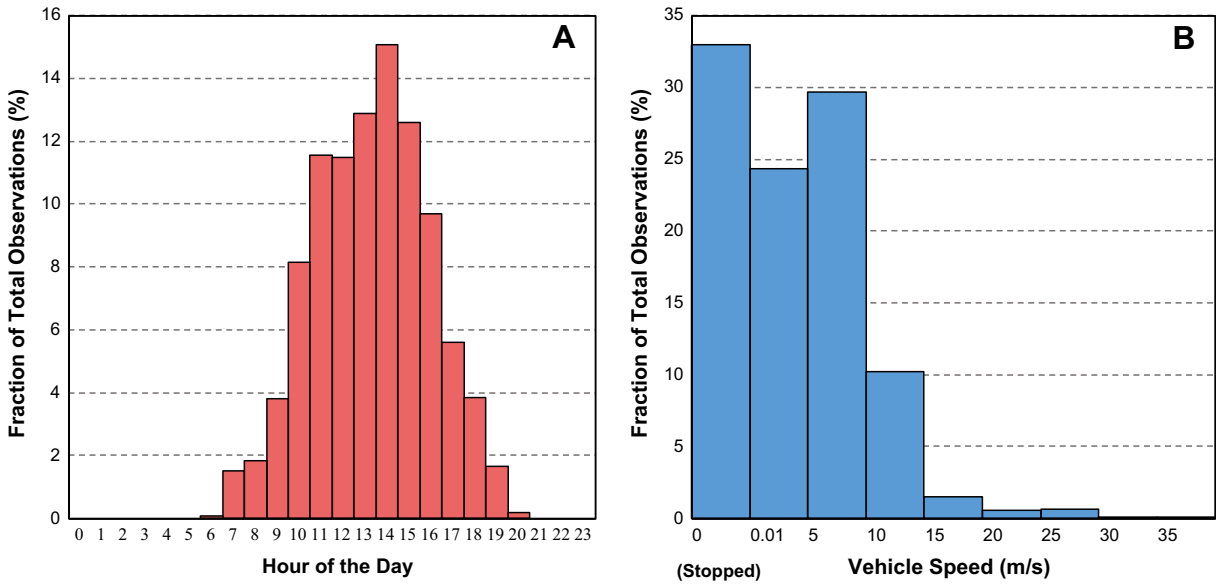

Fig. 5 Histograms showing fraction of observations collected by hour of day (A) and by vehicle speed (B)

and back wide-angle cameras) that measure both toxic and greenhouse gas pollutants, particulate matter, and other parameters. We detail the design, construction, and operation of MPAL and present results of tests that evaluated time lags of each instrument, PM inlet losses, and wind measurement accuracy. We developed an algorithm to obtain corrected PM concentrations as a function of driving speed and particle size range. The onboard wind speed and direction measurements are unbiased at lower vehicle speeds (< 15 m/s); we saw bias at higher speeds and on highways following large vehicles. Deployment over a 1-year period in southwest Detroit, Michigan, is a very large data set with high data completeness; average pollutant levels were comparable to levels collected at local regulatory sites.

We illustrated only a few preliminary analyses of MPAL data in this article. Analysis of the very rich dataset collected by MPAL is underway. These may include the following applications: peak finding algorithms that detect concentration and emission "hotspots," e.g., CH_4 peaks can show natural gas pipeline leaks; pollutant mapping to provide highly resolved exposure information; further analysis of collocation data to confirm quality of MPAL monitoring; evolution of PM size distributions and the formation of secondary pollutants (O_3 and $PM_{2.5}$); receptor modeling and source apportionment (potentially using the trace metal measurements obtained by the Horiba PX375); trends over time in pollutant maps; and exposure levels and the linkage to traffic patterns and industrial emissions, including the impact of the GHIB. Other potential applications may include detecting new emission sources, coupling the concentration maps to epidemiological or health impact analyses, environmental equity studies, and evaluation or verification of mitigation policies and actions.

Supplementary material The online version of this article (https://doi.org/10.1007/s10661-020-08769-2) contains supplementary material, which is available to authorized users.

Acknowledgments Support for this research was obtained from the State of Michigan under a contract entitled "Air Monitoring for the Gordie Howe International Bridge." Additional support was provided by grant P30ES017885 from the National Institute of Environmental Health Sciences, NIH. The content is solely the responsibility of the authors and does not necessarily represent the official views of the NIH. We appreciate the assistance of our laboratory and field staff, including Chris Godwin, Megan Bader, Han Tran, and Daniel Pert. We also acknowledge the support of Lauren Fink and the Detroit Health Department, Susan Kilmer, Navnit Ghuman, and Eric Hansen at the Michigan Department of Environment, Great Lakes and Energy, Jennifer Gray at the Michigan Department of Health and Human Services, Simone Sagovac at the Southwest Detroit Community Benefits Coalition, and Tim Wallington at the Ford Motor Company.

Funding Support for this research was obtained from the State of Michigan under a contract entitled "Air Monitoring for the Gordie Howe International Bridge." Additional support was provided by grant P30ES017885 from the National Institute of Environmental Health Sciences, NIH, and the Ford Motor Company.

Data availability The supplementary materials contain additional information and data pertinent to this article.

Compliance with ethical standards

Conflict of interest None.

Code availability Not applicable.

References

Adams, M. D., DeLuca, P. F., Corr, D., & Kanaroglou, P. S. (2012). Mobile air monitoring: Measuring change in air quality in the city of Hamilton, 2005–2010. *Social Indicators Research, 108*(2), 351–364.

Apte, J. S., Messier, K. P., Gani, S., Brauer, M., Kirchstetter, T. W., Lunden, M. M., Marshall, J. D., Portier, C. J., Vermeulen, R. C. H., & Hamburg, S. P. (2017). High-resolution air pollution mapping with Google street view cars: Exploiting big data. *Environmental Science & Technology, 51*(12), 6999–7008.

Baldauf, R. W., Isakov, V., Deshmukh, P., Venkatram, A., Yang, B., & Zhang, K. M. (2016). Influence of solid noise barriers on near-road and on-road air quality. *Atmospheric Environment, 129*, 265–276.

Bukowiecki, N., Dommen, J., Prevot, A., Richter, R., Weingartner, E., & Baltensperger, U. (2002). A mobile pollutant measurement laboratory—Measuring gas phase and aerosol ambient concentrations with high spatial and temporal resolution. *Atmospheric Environment, 36*(36–37), 5569–5579.

Chan, L., Lau, W., Zou, S., Cao, Z., & Lai, S. (2002). Exposure level of carbon monoxide and respirable suspended particulate in public transportation modes while commuting in urban area of Guangzhou, China. *Atmospheric Environment, 36*(38), 5831–5840.

Duncan, B. N., Prados, A. I., Lamsal, L. N., Liu, Y., Streets, D. G., Gupta, P., Hilsenrath, E., Kahn, R. A., Nielsen, J. E., Beyersdorf, A. J., Burton, S. P., Fiore, A. M., Fishman, J., Henze, D. K., Hostetler, C. A., Krotkov, N. A., Lee, P., Lin, M., Pawson, S., Pfister, G., Pickering, K. E., Pierce, R. B., Yoshida, Y., & Ziemba, L. D. (2014). Satellite data of atmospheric pollution for US air quality applications: Examples of applications, summary of data end-user resources, answers to FAQs, and common mistakes to avoid. *Atmospheric Environment, 94*, 647–662.

Eilerman, S. J., Peischl, J., Neuman, J. A., Ryerson, T. B., Aikin, K. C., Holloway, M. W., Zondlo, M. A., Golston, L. M., Pan, D., Floerchinger, C., & Herndon, S. (2016). Characterization of ammonia, methane, and nitrous oxide emissions from concentrated animal feeding operations in northeastern Colorado. *Environmental Science & Technology, 50*(20), 10885–10893.

Elen, B., Peters, J., Poppel, M. V., Bleux, N., Theunis, J., Reggente, M., et al. (2013). The Aeroflex: A bicycle for mobile air quality measurements. *Sensors, 13*(1), 221–240.

Fruin, S., Westerdahl, D., Sax, T., Sioutas, C., & Fine, P. (2008). Measurements and predictors of on-road ultrafine particle concentrations and associated pollutants in Los Angeles. *Atmospheric Environment, 42*(2), 207–219.

Global CH4 Monthly Means (2020). NOAA Global Monitoring Laboratory. https://www.esrl.noaa.gov/gmd/ccgg/trends_ch4/. Accessed 04/10/2020.

Hagler, G. S., Thoma, E. D., & Baldauf, R. W. (2010). High-resolution mobile monitoring of carbon monoxide and ultrafine particle concentrations in a near-road environment. *Journal of the Air & Waste Management Association, 60*(3), 328–336.

Hatzopoulou, M., Weichenthal, S., Dugum, H., Pickett, G., Miranda-Moreno, L., Kulka, R., Andersen, R., & Goldberg, M. (2013). The impact of traffic volume, composition, and road geometry on personal air pollution exposures among cyclists in Montreal, Canada. *Journal of Exposure Science & Environmental Epidemiology, 23*(1), 46–51.

Hernandez Bennetts, V., Lilienthal, A. J., Neumann, P., & Trincavelli, M. (2012). Mobile robots for localizing gas emission sources on landfill sites: Is bio-inspiration the way to go? *Frontiers in Neuroengineering, 4*, 20.

Kittelson, D. B., Watts, W. F., Johnson, J., Remerowki, M., Ische, E., Oberdörster, G., et al. (2004). On-road exposure to highway aerosols. 1. Aerosol and gas measurements. Inhalation Toxicology, 16(sup1), 31-39.

Lee, S., Kwak, J., Lee, S., & Lee, J. (2015). On-road chasing and laboratory measurements of exhaust particle emissions of diesel vehicles equipped with aftertreatment technologies (DPF, urea-SCR). *International Journal of Automotive Technology, 16*(4), 551–559.

Levy, I., Mihele, C., Lu, G., Narayan, J., & Brook, J. (2014a). Evaluating multipollutant exposure and urban air quality: Pollutant interrelationships, neighborhood variability, and nitrogen dioxide as a proxy pollutant. *Environmental Health Perspectives, 122*(1), 65–72.

Levy, I., Mihele, C., Lu, G., Narayan, J., Hilker, N., & Brook, J. (2014b). Elucidating multipollutant exposure across a complex metropolitan area by systematic deployment of a mobile laboratory. *Atmospheric Chemistry & Physics, 14*(14), 7173–7193.

Minet, L., Liu, R., Valois, M.-F., Xu, J., Weichenthal, S., & Hatzopoulou, M. (2018). Development and comparison of air pollution exposure surfaces derived from on-road mobile monitoring and short-term stationary sidewalk measurements. *Environmental Science & Technology, 52*(6), 3512–3519.

Monthly Average Mauna Loa CO2 (2020). NOAA Global Monitoring Laboratory. https://www.esrl.noaa.gov/gmd/ccgg/trends/index.html. Accessed 04/10/2020.

Ohio Department of Transportation - 2018 Facts Book (2018). http://www.dot.state.oh.us/Divisions/Planning/TechServ/Archived%20Fact%20Books/2018%20ODOT%20Facts%20Book.pdf. Accessed 2020.

Van den Bossche, J., Peters, J., Verwaeren, J., Botteldooren, D., Theunis, J., & De Baets, B. (2015). Mobile monitoring for mapping spatial variation in urban air quality: Development and validation of a methodology based on an extensive dataset. *Atmospheric Environment, 105*, 148–161.

von Fischer, J. C., Cooley, D., Chamberlain, S., Gaylord, A., Griebenow, C. J., Hamburg, S. P., Salo, J., Schumacher, R., Theobald, D., & Ham, J. (2017). Rapid, vehicle-based

identification of location and magnitude of urban natural gas pipeline leaks. *Environmental Science & Technology, 51*(7), 4091–4099.

Wallace, J., Corr, D., Deluca, P., Kanaroglou, P., & McCarry, B. (2009). Mobile monitoring of air pollution in cities: The case of Hamilton, Ontario, Canada. *Journal of Environmental Monitoring, 11*(5), 998–1003.

Wang, X., Westerdahl, D., Chen, L. C., Wu, Y., Hao, J., Pan, X., Guo, X., & Zhang, K. M. (2009). Evaluating the air quality impacts of the 2008 Beijing Olympic games: On-road emission factors and black carbon profiles. *Atmospheric Environment, 43*(30), 4535–4543.

Wang, X., Westerdahl, D., Wu, Y., Pan, X., & Zhang, K. M. (2011). On-road emission factor distributions of individual diesel vehicles in and around Beijing, China. *Atmospheric Environment, 45*(2), 503–513.

Wang, X., Westerdahl, D., Hu, J., Wu, Y., Yin, H., Pan, X., & Max Zhang, K. (2012). On-road diesel vehicle emission factors for nitrogen oxides and black carbon in two Chinese cities. *Atmospheric Environment, 46*, 45–55.

Weller, Z. D., Roscioli, J. R., Daube, W. C., Lamb, B. K., Ferrara, T. W., Brewer, P. E., & von Fischer, J. (2018). Vehicle-based methane surveys for finding natural gas leaks and estimating their size: Validation and uncertainty. *Environmental Science & Technology, 52*(20), 11922–11930.

Weller, Z. D., Yang, D. K., & von Fischer, J. C. (2019). An open source algorithm to detect natural gas leaks from mobile methane survey data. *PLoS One, 14*(2), e0212287.

Westerdahl, D., Fruin, S., Sax, T., Fine, P. M., & Sioutas, C. (2005). Mobile platform measurements of ultrafine particles and associated pollutant concentrations on freeways and residential streets in Los Angeles. *Atmospheric Environment, 39*(20), 3597–3610.

Westerdahl, D., Fruin, S. A., Fine, P. L., & Sioutas, C. (2008). The Los Angeles international airport as a source of ultrafine particles and other pollutants to nearby communities. *Atmospheric Environment, 42*(13), 3143–3155.

Westerdahl, D., Wang, X., Pan, X., & Zhang, K. M. (2009). Characterization of on-road vehicle emission factors and microenvironmental air quality in Beijing, China. *Atmospheric Environment, 43*(3), 697–705.

Wild, R. J., Dubé, W. P., Aikin, K. C., Eilerman, S. J., Neuman, J. A., Peischl, J., Ryerson, T. B., & Brown, S. S. (2017). On-road measurements of vehicle NO2/NOx emission ratios in Denver, Colorado, USA. *Atmospheric Environment, 148*, 182–189.

Yamada, H., Hayashi, R., & Tonokura, K. (2016). Simultaneous measurements of on-road/in-vehicle nanoparticles and NOx while driving: Actual situations, passenger exposure and secondary formations. *Science of the Total Environment, 563*, 944–955.